Journal of the European Ceramic Society 44 (2024) 254–260

Contents lists available at ScienceDirect

Journal of the European Ceramic Society

journal homepage: www.elsevier.com/locate/jeurceramsoc

Temperature-dependent dielectric properties and high-temperature microwave absorption performance of Ti_3SiC_2/Al_2O_3-13%TiO_2 coatings

Weichao Wang, Liuying Wang [*], Gu Liu [*], Chaoqun Ge, Long Wang, Bin Wang, Jie Huang

Zhijian Laboratory, Rocket Force University of Engineering, Xi'an 710025, China

A R T I C L E I N F O

Keywords:
MAX phase
High-temperature dielectric properties
High-temperature microwave absorbing properties
Plasma spraying

A B S T R A C T

Ti_3SiC_2 exhibits considerable potential for high-temperature microwave absorption due to its relatively high melting point and conductivity. In this study, we successfully prepared Ti_3SiC_2/Al_2O_3-13%TiO_2 heterogeneous coatings through granulation and plasma spraying techniques. This investigation covered composition, microstructure, oxidation resistance, and a focused analysis of the temperature-dependent permittivity of the coatings. The augmentation in Ti_3SiC_2 content leads to an escalation in the polarized component, consequently elevating susceptibility to dielectric dispersion. With rising temperature, polarization within the coatings gradually establishes, prompting a transition from polarization relaxation loss to conduction loss as the dominant dielectric loss mechanism. At 5 wt% Ti_3SiC_2 content, the coating achieves an effective bandwidth of 2.2 GHz at 873 K, with a mere 1.4 mm thickness. Moreover, the coating maintains exceptional oxidation resistance below 700 °C. Ti_3SiC_2/Al_2O_3-13%TiO_2 coatings manifest as strong contenders for high-temperature microwave absorption applications, and plasma spraying emerges as a promising technique for fabricating high-performance microwave absorption coatings.

1. Introduction

Microwave absorbing materials (MAMs), as specialized functional materials, play a pivotal role in mitigating electromagnetic pollution [1,2]. Despite decades of utilization across various applications, the broader operational scope of MAMs remains constrained by their inherent attributes. Among diverse absorbing materials, including carbonyl iron absorbing materials [3,4], carbon absorbing materials [5,6], and conductive polymer absorbing materials [7,8], the utilization is hindered by their notably low Curie temperature or oxidation temperature, rendering them unsuitable for high-temperature environments [9]. Consequently, exploring MAMs tailored for harsh environments has emerged as an imperative avenue of research across civil, commercial, military, and aerospace sectors.

Silicon-based materials, including SiC, SiC_f, SiCN, SiBCN, Si_3N_4, are frequently adopted for high-temperature applications due to their elevated melting point and commendable chemical stability [10–14]. However, the microwave loss capacity of these materials often falls short, necessitating substantial thickness to achieve impedance matching and optimal loss conditions. The demand for significant thickness poses considerable challenges in practical applications, thereby increasing the complexity of employing high-temperature absorption materials. Consequently, the exploration of MAMs combining high-temperature resistance, substantial electromagnetic loss, and suitability for coating preparation techniques gains paramount importance.

In order to consider both electromagnetic loss and high temperature resistance, MAX phase material seems to be a promising candidate. MAX material ($M_{n+1}AX_n$: M = transition metals, A = Third or fourth main group element, X = C or N, n = 1–3) possesses hexagonal layered structure, which is composed of M_6X layer and A atom layer alternately [15]. MAX materials have garnered substantial interest from researchers due to their noteworthy combination of metallic electrical and thermal conductivity, in conjunction with ceramic attributes of oxidation resistance and resistance to corrosion [16]. The distinctive properties of MAX phase materials offer valuable insights for the formulation of microwave-absorbing coatings with enhanced performance. Notably, among these materials, Ti_3SiC_2 exhibits impressive qualities such as oxidation resistance, elevated mechanical strength, favorable machinability, and noteworthy plasticity. Furthermore, Ti_3SiC_2 demonstrates exceptional electrical conductivity, leading to the development of substantial dielectric loss capacity, setting it apart from conventional ceramic materials [17]. Based on this, Ti_3SiC_2 has potential application

---

* Corresponding authors.
E-mail addresses: lywangxa@163.com (L. Wang), liugu5032@163.com (G. Liu).

https://doi.org/10.1016/j.jeurceramsoc.2023.08.032
Received 8 May 2023; Received in revised form 18 August 2023; Accepted 19 August 2023

in harsh environments microwave absorption. To further fortify Ti_3SiC_2 against performance deterioration in high-temperature settings, careful attention is directed toward the substrate of the absorbing materials. The integration of Ti_3SiC_2 with Al_2O_3-13%TiO_2 (AT13) insulating ceramic presents notable advantages, including high hardness, chemical stability, wear resistance, and corrosion resistance, making it extensively employed in aerospace, petrochemical, and other demanding domains [18,19]. The amalgamation of AT13 and Ti_3SiC_2 holds promise in enhancing impedance matching while concurrently elevating Ti_3SiC_2's oxidation decomposition temperature, thereby expanding the materials' operational temperature range. Notably, plasma spraying, due to its high operating temperatures and oxygen-free environments, emerges as a propitious technique for high-temperature microwave absorption applications. This technique facilitates the rapid formation of high-melting point materials such as ceramics and metals, as well as materials with limited oxidation resistance, including carbon-based and polymer materials [20,21].

In this study, we present a methodology wherein Ti_3SiC_2, renowned for its exceptional dielectric properties, is consolidated into powder form with AT13 using a simple, efficient, and economical granulation technique (no specialized equipment required). Subsequent application of plasma spraying culminates in Ti_3SiC_2/AT13 high-temperature microwave absorption coatings. Our exploration investigates the impact of granulation and spraying processes on the coatings' crystal structure, morphology, and oxidation resistance. Concurrently, we scrutinize the temperature-dependent permittivity and high-temperature microwave absorption properties of Ti_3SiC_2/AT13 coatings. The findings underscore the exemplary high-temperature resistance and microwave absorption performance of Ti_3SiC_2/AT13 coatings, even at limited thicknesses, suggesting broad prospects for industrial applications.

2. Material and methods

Plasma-sprayed powder was derived from the agglomeration and granulation of high-purity powders of Ti_3SiC_2 (Jilin 11 Technology Co., Ltd, China, >99.9 %) and AT13 (Oerlikon Metco Co., Ltd, USA). Ti_3SiC_2 powder was blended with AT13 powder in mass percentages of 0 %, 3 %, 5 %, and 7 % to create a starting powder. Polyvinyl alcohol (PVA, 80.0–110.0 mPa·s), used solely as an adhesive, was sourced from Shanghai Aladdin Company. PVA was dissolved in 90 °C deionized water at a concentration of 80 g/L, followed by magnetic stirring until a clear solution was achieved. The starting powders were mixed with the PVA solution at a powder: liquid mass ratio of 4:1 to form a paste, subsequently ground for 30 min. The resulting paste was dried at 150 °C for 12 h, and then finely powdered with particle sizes ranging between 50 and 100 μm. The plasma-sprayed powder derived from the four components was labeled as T0, T3, T5, and T7. This finely prepared powder was employed to fabricate Ti_3SiC_2/AT13 absorbing coatings using plasma spray technology. Primary and auxiliary plasma-forming gases included argon (19 slpm) and nitrogen (1 slpm), respectively. The carrier gas, nitrogen (5 slpm), was utilized to feed powder at a rate of approximately 20 g/min. Plasma arc current and voltage were fixed at 250 A and 30 V, respectively. The spraying distance was maintained at 100 mm. The process of coating preparation is depicted in Fig. S1.

The phase structure was characterized using X-ray diffraction (XRD, Bruker D8 Advance) with Cu Kα irradiation ($\lambda = 1.540598$ Å) at 40 kV and 40 mA. Data were collected within 2θ angles spanning 10–90°, employing a step size of 0.017°. Microstructure and chemical compositions were analyzed through a Hitachi SU5000 scanning electron microscope (SEM), outfitted with an energy-dispersive spectroscopy (EDS) detector. The temperature-dependent electrical properties of the coatings, within the range of 300–973 K, were evaluated using a Physical Property Measurement System (PPMS, Quantum Design PPMS-9). Thermogravimetric analysis (TGA) and differential scanning calorimetry (DSC) were performed using a Mettler-Toledo TGA/DSC analyzer from 25° to 700°C, at a heating rate of 10 °C·min^{-1} under an air environment.

Temperature-dependent permittivity of the coatings was determined via the waveguide method. The procedure involved uniform spraying of plasma-sprayed powder onto an aluminum substrate, followed by separation of the coating from the substrate, and subsequent cutting into rectangular blocks measuring 22.86 × 10.16 × 2 mm. Electromagnetic parameter testing, employing a vector network analyzer (VAN, Ceyear 3672c) and a microwave heating furnace, was employed to assess the temperature-dependent permittivity of the coatings within the frequency range of 8.2–12.4 GHz. During the test, furnace temperature ranged from 300 to 973 K, with the furnace's heating rate maintained at 10 K/min.

3. Results and discussion

3.1. Crystal structure

Fig. S2 displays the XRD patterns for commercially available Ti_3SiC_2 and AT13 powders. The observed reflections can be indexed as the presence of small quantities of Ti_2Si_3 and Al_2TiO_5. Fig. 1 shows XRD patterns for Ti_3SiC_2/AT13 absorbing coatings. The appearance of diffraction peaks corresponding to Ti_3SiC_2 implies that the plasma spraying process did not induce significant decomposition of Ti_3SiC_2. Notably, the primary phase for T0 coating is identified as spinel-structured γ-Al_2O_3 (JCPDS: #29–0063); in contrast, for other coatings prepared by agglomerating Ti_3SiC_2 and AT13, the main phase is α-Al_2O_3 with space group R-3c (JCPDS: #10–0173). This distinction arises from the lower interfacial energy of γ-Al_2O_3 compared to α-Al_2O_3. During the process of melting and deposition of AT13, the initial formation of γ-Al_2O_3 crystal nucleus occurs due to its lower surface energy [22,23]. In the absence of agglomeration and granulation, rapid cooling leads to substantial undercooling of the crystal nucleus, accelerating nucleation and promoting γ-Al_2O_3 formation. Additionally, the thermodynamics of Al_2O_3's phase transition suggests that γ-Al_2O_3 tends to transform into α-Al_2O_3 upon exposure to elevated temperatures [24,25]. Consequently, after agglomeration and granulation, Ti_3SiC_2 particles act as buffers, hindering heat transfer and fostering the conversion of γ-Al_2O_3 to α-Al_2O_3. In cases where plasma spraying is used for Al_2O_3-TiO_2 coatings, deoxidation of TiO_2 often occurs, forming the amorphous TiO_{2-x} [26]. Hence, the TiO_2 phase is challenging to identify in the T0 coating. However, the diffraction peaks of rutile TiO_2 (JCPDS: #21–1276) can be discerned in the XRD patterns of the remaining coatings, owing to the buffering effect of Ti_3SiC_2. Concurrently, the emergence of the new TiC phase is attributed to insufficient oxygen partial pressure during plasma spraying, causing Ti_3SiC_2 decomposition and TiC formation [27].

3.2. Microstructural analysis

The micromorphology of T7 composite absorbing materials

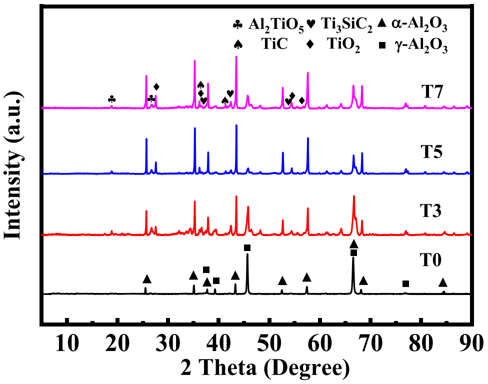

Fig. 1. XRD patterns of Ti_3SiC_2/AT13 microwave absorption coatings.

following granulation is presented in Fig. 2(a). The particle size distribution ranges between 30 and 50 μm, displaying uniform shape and significant spheroidization. Spheroidization degree crucially affects powder fluidity, which impacts the spraying process continuity and resulting coating quality. Upon magnification, spherical particles are found to be composed of smaller irregular particles, implying uniform dispersion and bonding of the two materials via granulation. This achieves simultaneous deposition of absorber and substrate during spraying.

The microstructural analysis of the T7 composite absorber material after plasma spraying is depicted in Fig. 2(b). The spherical particles exhibit a more uniform, smooth, and compact appearance, indicating the adequate heating and melting of the plasma-sprayed powder in the ultra-high temperature plasma flame flow. Notably, the ceramic material Ti_3SiC_2 possesses a melting point of 3000 °C, surpassing that of Al_2O_3 (2054 °C) and TiO_2 (1840 °C) [28]. As such, within the high-speed plasma plume, the matrix AT13 was initially molten and subsequently evenly applied onto the particle surfaces, forming a protective layer. The creation of this protective layer proves beneficial in elevating the oxidative decomposition temperature of Ti_3SiC_2. EDS mapping (Fig. 2(c, d)) confirms the even distribution of Si and C elements on particle surfaces, validating the efficiency of the granulation procedure employed. The process of forming the Ti_3SiC_2 buffer layer and AT13 protective layer is illustrated in Fig. S1.

To preliminarily assess the application impact, T7 composite absorber materials were applied to 45 steel through spraying, resulting in a coating whose end surface morphology is depicted in Fig. 2(e). The illustration underscores the robust adherence of the coating to the substrate, exhibiting a high density and no discernible detachment. Additionally, SEM images of the end surface highlight noticeable variations in chromaticity. Specifically, the white dashed line in the image signifies localized melting of Ti_3SiC_2. Evidently, the EDS mapping in Fig. 2(f) provides evidence of this composition distinction in these regions. The molten Ti_3SiC_2 region in the coating can be readily identified based on the distribution of Ti, Si, Al, and O elements in the EDS images. Furthermore, the presence of voids and porosity in the coating can be attributed to incomplete particle melting during the spraying process. Such voids and porosity can yield dual effects: affecting the coating's mechanical traits, while concurrently intensifying the repetitive reflection and scattering of electromagnetic waves. Numerous studies have reported that the repeated reflection and scattering due to a porous structure greatly contribute to effective electromagnetic wave absorption [29,30]. The morphology of the remaining samples post-agglomeration, spraying, and coating end surface are depicted in Fig. S4.

3.3. Oxidation behavior

The material's capacity to withstand oxidation at elevated temperatures is a critical precondition for its service in high-temperature settings. To investigate the coatings' dependable operational temperatures, synchronized thermogravimetric analysis of T7 samples was conducted before and after plasma spraying. For convenience, we label the T7 before and after plasma spraying as the T7-NS and T7-S, respectively.

DSC heat flow curves for T7-NS, as depicted in Fig. 3(a), reveal an uninterrupted exothermic process throughout heating. Notably, as the temperature surpasses 587 °C, a more potent exothermic trend emerges, persisting even at the highest temperature. This underscores the continuous oxidative decomposition of Ti_3SiC_2 during superheating. Conversely, T7-S's heat flow is minimal, implying a relatively sluggish oxidation rate for Ti_3SiC_2.

Fig. 3(b) presents the variation in sample weight with increasing temperature. The weight alteration of T7-NS can be discerned across three distinct stages with rising temperature: i) below 220 °C, negligible weight change alongside a stable sample state; ii) between 220 and 434 °C, slight weight reduction primarily due to PVA decomposition; and iii) above 434 °C, evident weight increase due to the oxidative decomposition of Ti_3SiC_2. Over the entire heating process, the T7-NS sample's weight increases by roughly 7 %. In contrast, post-plasma spraying, the T7-S sample's weight gain at 700 °C is 0.64 %. Beyond 700 °C, a notable weight increase is witnessed, resulting in an approximate 6 % weight gain for the T7-S sample. Consequently, modification solely through agglomeration granulation without plasma spraying has minimal effect on oxidation resistance. Post-plasma spraying, the sample remains stable under 700 °C, exhibiting a 266 °C increase in the onset temperature of oxidation. This substantiates the efficacy of the plasma spraying process in enhancing the oxidation resistance of the Ti_3SiC_2/AT13 composite material, thus broadening its operational temperature range.

3.4. High-temperature conductivity and dielectric properties

For nonmagnetic materials, their electromagnetic characteristics are fundamentally described by complex permittivity (ε' and ε''). By the

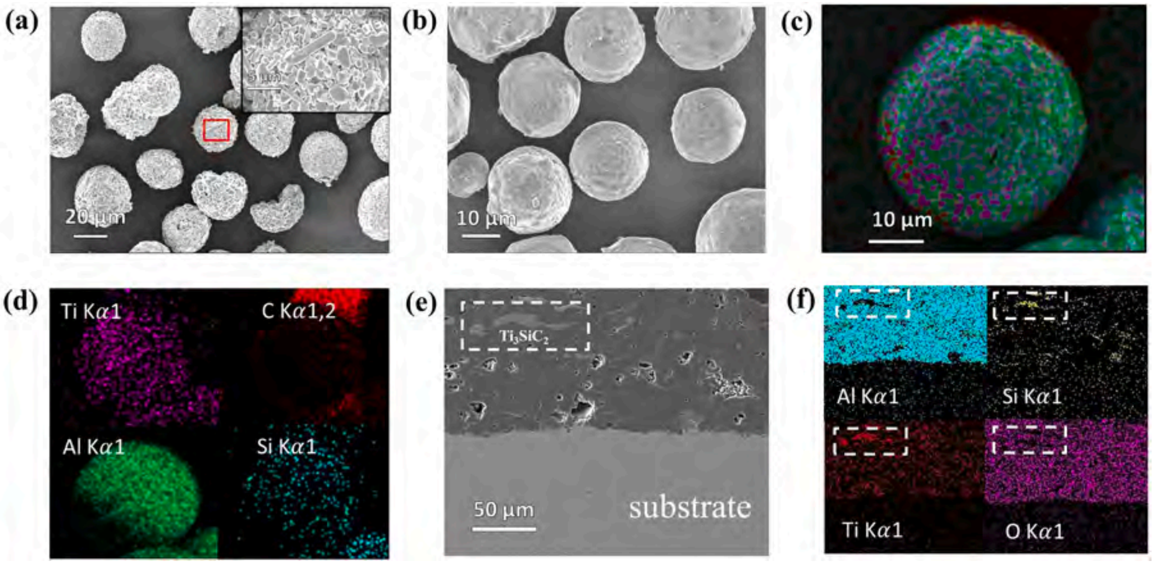

Fig. 2. SEM images of Ti_3SiC_2/AT13 composite materials after (a) granulation and (b) plasma spraying respectively. (c, d) EDS mappings of Ti_3SiC_2/AT13 composite materials after plasma spraying. (e) SEM images of T7 coating. (f) EDS mappings of T7 coating.

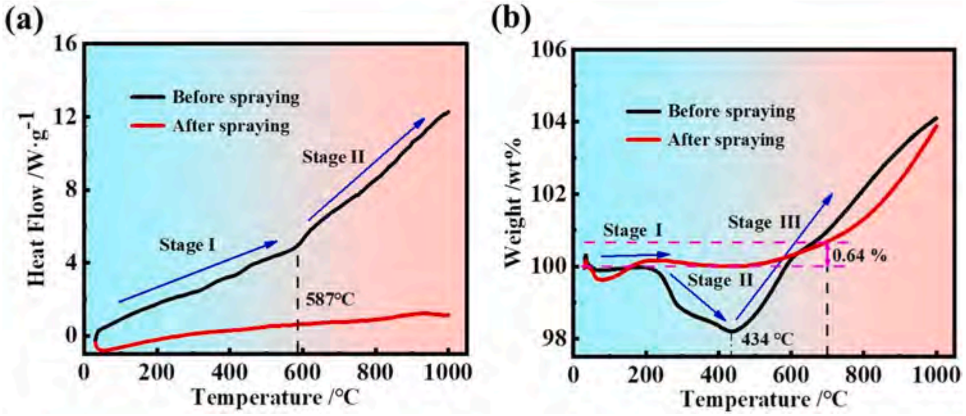

Fig. 3. (a) DSC and (b) TG curves of T7 composite materials before and after plasma spraying.

modified Debye Relaxation theory (the explicit formulas are described in the Supplementary Information), ε'' is composed of ε''_P and ε''_c, where ε''_P is contributed by the polarization relaxation loss and ε''_c by the conductance loss. To explore electronic attributes, particularly temperature-dependent dielectric properties, high-temperature conductivity testing was conducted on Ti_3SiC_2/AT13 coatings. Fig. 4(a) illustrates the temperature-dependent conductivity variation as measured by PPMS. Evidently, the coatings' conductivity demonstrates a semiconductor-like increase with temperature. However, numerous studies have established Ti_3SiC_2's metallic character, a typical trait of MAX phase materials, marked by valence and conduction bands significantly overlapping [31,32]. As such, Ti_3SiC_2 should exhibit a positive resistivity temperature coefficient, indicating that conductivity decreases with temperature—an opposite trend to that exhibited by the coatings. Remarkably, the semiconductor properties and negative temperature coefficient of resistivity in Al_2O_3 and TiO_2 have been extensively documented [33,34]. Furthermore, considering the proportion of Ti_3SiC_2 in the coating is notably less than that of AT13, it is proposed that the augmented conductivity of the AT13 matrix plays a pivotal role in the observed elevation of coating conductivity with temperature.

To investigate coatings' high-temperature dielectric properties, variations in permittivity with temperature were measured through in situ heating VAN. Fig. 4(b, c) graphically presents the dielectric characteristics of the T3 and T5 coatings within the X-band at varying temperatures. Corresponding information on the temperature-dependent permittivity of the T0 and T7 coatings is available in Fig. S5. Based on Equation (S1), elevating the temperature results in a reduction of relaxation time τ(T), thereby causing ε' to exhibit a noticeable increase. As the temperature escalates, the ε' of all coatings demonstrates a gradual increase, as depicted in Fig. 4(b_1, c_1). However, a noteworthy aspect concerns the behavior of ε'' in response to temperature changes. Referring to Fig. S5(a_2) and Fig. 4(b_2), it is observable that the value of ε'' for both the T0 and T3 coatings gradually ascends with temperature but experiences a gradual decline as frequency increases. Equation (S2) and Equation (S3) suggest that at lower temperatures, when τ(T) is relatively large, $\omega\tau(T)\gg 1$. In such cases, ε'' can be transformed into:

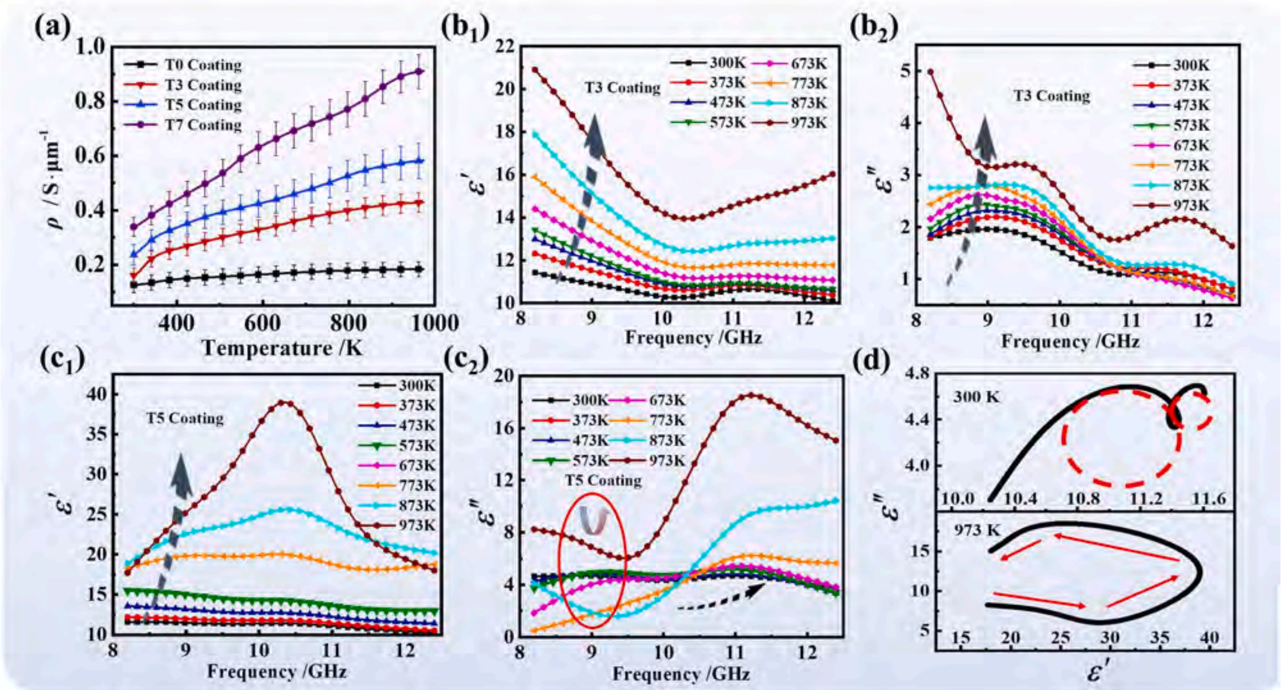

Fig. 4. (a) Temperature-dependent conductivity of Ti_3SiC_2/AT13 microwave absorption coatings. The temperature-dependent (b_1, c_1) ε' and (b_2, c_2) ε'' as function of frequency for T3 and T5 coatings. (d) Cole-Cole plots of complex permittivity for T5 coating at 300 K and 973 K.

$$\varepsilon'' = \frac{\varepsilon_s - \varepsilon_\infty}{\omega\tau(T)} + \frac{\sigma(T)}{\omega\varepsilon_0} \tag{1}$$

As temperature rises, τ(T) diminishes as σ(T) augments, leading to a conspicuous increase in ε''. Additionally, with the increase of ω, both ε''_P and ε''_c undergo a reduction, resulting in a gradual decline in ε''. However, due to the increased presence of Ti_3SiC_2 in the coating, the polarization stemming from dipoles, defects, and interfaces increases. This divergence causes the ε'' behavior of T5 and T7 coatings to markedly differ from that of T0 and T3 coatings. As shown in Fig. 4(c_2), the ε'' of T5 coatings initially decreases, then increases with the increasing temperature. This phenomenon can be attributed to several factors. Firstly, based on Equation (S2), an increased temperature exponentially decreases τ(*T*), prompting $\omega\tau(T)$ to transition from $\gg 1$ to ≈ 1, and then further transitioning to $\ll 1$. The resulting in the transformation of ε''_P as follows [35–37]:

$$\varepsilon''_p = (\varepsilon_s - \varepsilon_\infty)\omega\tau(T) \tag{2}$$

In this process, ε_P' reaches its maximum value of $\frac{\varepsilon_s - \varepsilon_\infty}{2}$ when $\omega\tau(T) = 1$, it is referred to as the dielectric dispersion region. Subsequently, according to the Schweidler equation, when various polarized components possessing similar τ(T) exist within the dielectric, the dispersion region expands [36,38,39]. Consequently, coatings like T5 and T7, which contain numerous polarized components, are more susceptible to experiencing dispersion. With escalating temperature, these coatings are prone to crossing the dispersion region. Accordingly, as per Eq. (2), a decrease in τ(T) corresponds to a decrease in ε''_P. The gradual decline of ε''_P from a microscopic perspective results from intensified thermal motion of dipoles, which aligns with the external electric field, thereby diminishing polarization loss ability. While the establishment of polarization reduces the significance of polarization loss, the substantial increase in σ(T) with temperature magnifies the prominence of conduction loss as a dominant mechanism. This transition is confirmed by the Cole-Cole plots in Fig. 4(d). At 300 K, two distinct semi-circles on the curve correspond to two relaxation processes, whereas at 973 K, the curve is primarily composed of straight lines. This competitive interplay between polarization and conductivity results in an initial decline followed by an increase in ε''. In summary, at lower temperatures, polarization loss governs, leading to a gradual reduction in ε'' due to polarization establishment. Conversely, at higher temperatures, the marked conductivity increase results in conduction loss prevailing, leading to a gradual ε'' rise in tandem with conductivity growth. Additionally, the ε'' of T5 and T7 coatings exhibits a different trend compared to T0 and T3 coatings as the frequency increases. According to Eq. (2), higher frequencies contribute to greater polarization loss; thus, leading to a progressive elevation of ε'' with increasing frequency.

3.5. *High-temperature microwave absorption properties*

To assess the high-temperature microwave absorption characteristics of the Ti_3SiC_2/AT13 coatings, according to the transmission line theory, the reflectivity loss (*RL*) of the coatings were evaluated by the following equations [12]:

$$Z_{in} = Z_0\sqrt{(\mu_r/\varepsilon_r)}tanh\left[j\left(2\pi fd\Big/c\right)\sqrt{(\mu_r\varepsilon_r)}\right] \tag{3}$$

$$RL = 20lg|(Z_{in} - Z_0)/(Z_{in} + Z_0)| \tag{4}$$

where *f* denotes the electromagnetic wave frequency, *d* represents the material thickness, and Z_{in} is the input impedance at the absorber-air interface, which is linked to complex permeability and complex permittivity. For an ideal absorber, Z_{in} equals 1.

Fig. 5(a, b) visually illustrates the reflectivity loss of T3 and T5 coatings at various thicknesses and temperatures. For T3 coatings, an effective bandwidth ($RL < -10$ dB) of 1.9 GHz is attainable at a thickness of 2.0 mm and a temperature of 973 K, while a bandwidth exceeding 3 GHz (with $RL < -5$ dB) is feasible. With a T3 coating thickness of 2.5 mm, the bandwidth with $RL < -5$ dB surpasses 2 GHz within the temperature range of 300–873 K. As for the T5 coating, at a thickness of 1.4 mm and a temperature of 873 K, an effective bandwidth of 2.2 GHz is achieved, expanding to 3.0 GHz for RL < –5 dB when the temperature hits 973 K. Notably, the T5 coating exhibits substantial bandwidths at multiple temperatures with a thickness of 2.2 mm. Specifically, effective bandwidths span from 3.37 GHz at 300 K to 2.12 GHz at 573 K. The minimum *RL* value reaches 48.2 dB at 373 K and 51.8 dB at 573 K. Analysis of the Ti_3SiC_2/AT13 coatings' microstructure and permittivity underscores their impressive microwave absorption potential, attributed to the synergy of diverse microwave absorption mechanisms. These encompass the favorable electrical conductivity of Ti_3SiC_2 and the polar centers induced by defects, enhancing the

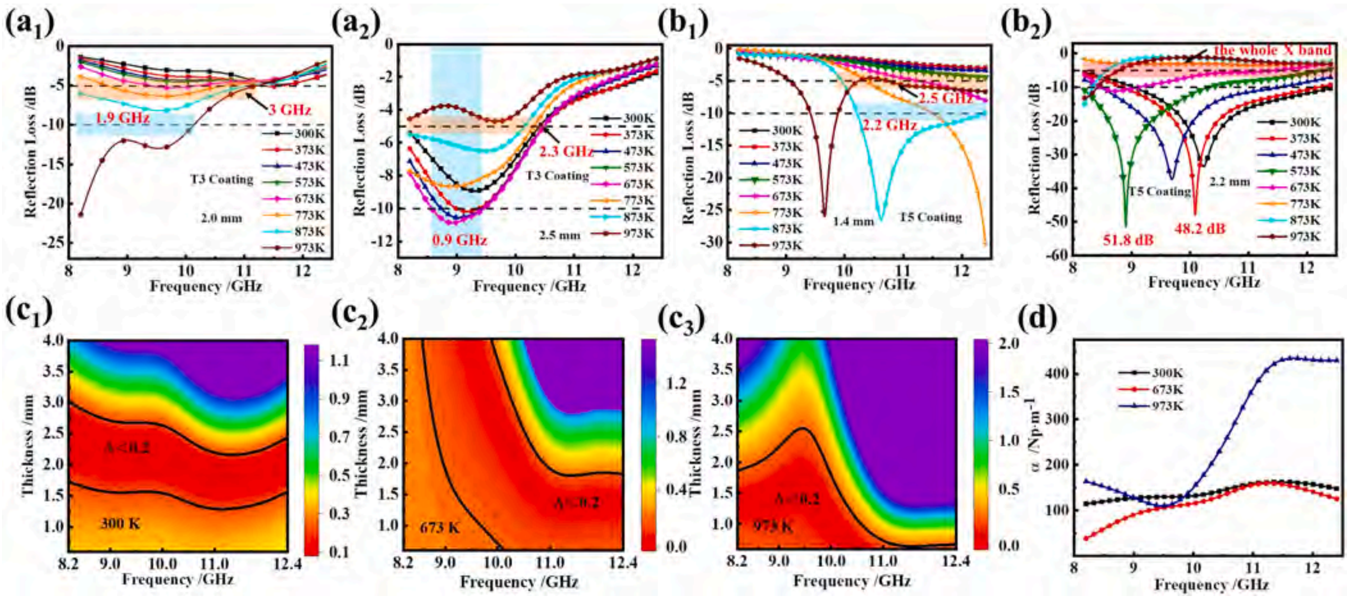

Fig. 5. Reflectivity loss of (a_1, a_2) T3 and (b_1, b_2) T5 coatings with varying thicknesses across temperatures from 300 K to 973 K. Impedance matching factor (c_1, c_2, c_3) and attenuation constant (d) of the T5 coating at 300 K, 773 K, and 973 K are presented.

coating's conductivity and dipole polarization loss capabilities [40,41]. The non-uniform charge distribution between Ti_3SiC_2 and the AT13 matrix within the coating leads to interface polarization loss. Moreover, the existence of holes and porosity within the coatings promotes repeated reflection and scattering of microwaves within the coating [42, 43].

To explore further the influence of temperature on electromagnetic wave absorption, we introduce the impedance matching factor and attenuation constant. The absorption performance of a material is determined by its impedance matching performance and attenuation constant. The former determines whether electromagnetic waves can enter the interior of the materials as much as possible, while the latter denotes the material's loss ability toward electromagnetic waves. The attenuation constant (α) of a material is formulated as follows [44]:

$$\alpha = \frac{\sqrt{2}\pi f}{c}\sqrt{\mu''\varepsilon'' - \mu'\varepsilon' + \sqrt{(\mu'^2 + \mu''^2)(\varepsilon'^2 + \varepsilon''^2)}} \tag{5}$$

Impedance matching performance can be expressed by impedance matching factor (Δ) [45]:

$$\Delta = \left|\sinh^2(Kfd) - M\right| \tag{6}$$

A value of Δ approaching zero signifies better impedance matching performance. Based on the above formulas, Fig. 5(c, d) shows the attenuation constant and impedance matching factor of the T5 coating at 300 K, 673 K, and 937 K. The regions exhibiting improved impedance matching ($\Delta < 0.2$) gradually shift toward lower frequencies and smaller thicknesses with rising temperature. Therefore, the reflectance peak shifts toward lower frequency with temperature elevation. Regrettably, the low attenuation constant impedes effective microwave loss, due to the inherent trade-off between impedance matching and attenuation constant. The mismatch between impedance and attenuation often hampers materials from achieving ideal absorption properties in high-temperature conditions. The analysis underscores the outstanding microwave absorption performance of the plasma-sprayed Ti_3SiC_2/AT13 coatings in high-temperature environments. It is imperative, however, to judiciously adjust the Ti_3SiC_2 content and coating thickness according to the target temperature and desired microwave absorption properties during the design and optimization of these coatings.

4. Conclusions

In summary, a series of high-temperature resistant Ti_3SiC_2/AT13 microwave absorbing coatings have been successfully devised and produced through the application of plasma spraying. The granulation spraying technique has demonstrably improved the coatings' resistance to oxidation, yielding commendable thermal stability under 700 °C. Our investigation into the temperature-dependent permittivity of the coatings has unveiled the establishment of dielectric polarization and the consequent transition in the loss mechanism. As temperature rises, the primary dielectric loss mechanism in the coating transitions from polarization loss to conductive loss. This transition in the loss mechanism enables the coatings to maintain excellent microwave absorption performance even in high-temperature environments. The T5 coating maintains a respectable effective bandwidth ($RL < -10$ dB) of 2.2 GHz at 873 K, with a mere thickness of 1.4 mm. Even at 973 K, a bandwidth with $RL < -5$ dB can extend to 2.9 GHz. This study examines the evolutionary mechanism of the temperature-frequency characteristics of the dielectric constant in high-temperature absorbing materials, offering novel insights and approaches for the design of such materials. By analyzing the temperature-frequency characteristics of the coatings' permittivity, this study offers new insights for the design of high-temperature absorbing materials.

Declaration of Competing Interest

The authors declare that they have no known competing financial interests or personal relationships that could have appeared to influence the work reported in this paper.

Data availability

No data was used for the research described in the article.

Acknowledgements

This work was supported by Natural Science Basic Research Program of shannxi (No. 2022JQ-356); China Postdoctoral Science Foundation (2022M723884); Special Support Program for High-level Talents of Shaanxi Province (No. 2020-44). We also thank The Youth Innovation Team of Shaanxi Universities for the guidance on methodology.

Appendix A. Supporting information

Supplementary data associated with this article can be found in the online version at doi:10.1016/j.jeurceramsoc.2023.08.032.

References

[1] Q. An, D. Li, W. Liao, T. Liu, D. Joralmon, X. Li, J. Zhao, A. Novel Ultra-wideband, Electromagnetic wave-absorbing metastructure inspired by bionic gyroid structures, Adv. Mater. (2023), e2300659, https://doi.org/10.1002/adma.202300659.

[2] J. Wang, L. Liu, S. Jiao, K. Ma, J. Lv, J. Yang, Hierarchical carbon fiber@MXene@MoS_2 core-sheath synergistic microstructure for tunable and efficient microwave absorption, Adv. Funct. Mater. 30 (45) (2020), 2002595, https://doi.org/10.1002/adfm.202002595.

[3] K.S. Sista, S. Dwarapudi, D. Kumar, G.R. Sinha, A.P. Moon, Carbonyl iron powders as absorption material for microwave interference shielding: a review, J. Alloys Compd. 853 (2021), 157251, https://doi.org/10.1016/j.jallcom.2020.157251.

[4] Y. Zuo, X. Su, X. Li, Z. Yao, T. Yu, J. Zhou, J. Li, J. Lu, J. Ding, Multimaterial 3D-printing of graphene/$Li_{0.35}Zn_{0.3}Fe_{2.35}O_4$ and graphene/carbonyl iron composites with superior microwave absorption properties and adjustable bandwidth, Carbon 167 (2020) 62–74, https://doi.org/10.1016/j.carbon.2020.05.071.

[5] Z. Zhang, Z. Xiong, Y. Yao, D. Wang, Z. Yang, P. Zhang, Q. Zhao, W. Zhou, Constructing conductive network in hybrid perovskite for a highly efficient microwave absorption system, Adv. Funct. Mater. 32 (39) (2022), 2206053, https://doi.org/10.1002/adfm.202206053.

[6] D. Liu, L. Yang, F. Wang, H. Zhang, J. Liu, T. Lv, H. Zhao, Y. Du, Hierarchical carbon nanotubes@Ni/C foams for high-performance microwave absorption, Carbon 196 (2022) 867–876, https://doi.org/10.1016/j.carbon.2022.05.057.

[7] Y. Jiao, F. Wu, A. Xie, L. Wu, W. Zhao, X. Zhu, X. Qi, Electrically conductive conjugate microporous polymers (CMPs) via confined polymerization of pyrrole for electromagnetic wave absorption, Chem. Eng. J. 398 (2020), 125591, https://doi.org/10.1016/j.cej.2020.125591.

[8] M. Wang, X.-H. Tang, J.-H. Cai, H. Wu, J.-B. Shen, S.-Y. Guo, Construction, mechanism and prospective of conductive polymer composites with multiple interfaces for electromagnetic interference shielding: a review, Carbon 177 (2021) 377–402, https://doi.org/10.1016/j.carbon.2021.02.047.

[9] Y. Jia, M.A.R. Chowdhury, D. Zhang, C. Xu, Wide-band tunable microwave-absorbing ceramic composites made of polymer-derived sioc ceramic and in situ partially surface-oxidized ultra-high-temperature ceramics, ACS Appl. Mater. Interfaces 11 (49) (2019) 45862–45874, https://doi.org/10.1021/acsami.9b16475.

[10] X. Yuan, L. Cheng, S. Guo, L. Zhang, High-temperature microwave absorbing properties of ordered mesoporous inter-filled SiC/SiO_2 composites, Ceram. Int. 43 (1) (2017) 282–288, https://doi.org/10.1016/j.ceramint.2016.09.151.

[11] T. Han, R. Luo, G. Cui, L. Wang, Effect of SiC nanowires on the high-temperature microwave absorption properties of SiC_f/SiC composites, J. Eur. Ceram. Soc. 39 (5) (2019) 1743–1756, https://doi.org/10.1016/j.jeurceramsoc.2019.01.018.

[12] X. Guo, Y. Feng, X. Lin, Y. Liu, H. Gong, Y. Zhang, The dielectric and microwave absorption properties of polymer-derived SiCN ceramics, J. Eur. Ceram. Soc. 38 (4) (2018) 1327–1333, https://doi.org/10.1016/j.jeurceramsoc.2017.10.031.

[13] Q. Chen, D. Li, X. Liao, Z. Yang, D. Jia, Y. Zhou, R. Riedel, Polymer-derived lightweight SiBCN ceramic nanofibers with high microwave absorption performance, ACS Appl. Mater. Interfaces 13 (29) (2021) 34889–34898, https://doi.org/10.1021/acsami.1c07912.

[14] F. Yang, J. Xue, Y. Ma, X. Li, X. Fan, S. Fan, Q. Zeng, L. Cheng, Sandwich structure SiC_f/Si_3N_4–SiOC–Si_3N_4 composites for high-temperature oxidation resistance and microwave absorption, Ceram. Int. 48 (17) (2022) 24803–24810, https://doi.org/10.1016/j.ceramint.2022.05.130.

[15] J. Haemers, R. Gusmão, Z. Sofer, Synthesis protocols of the most common layered carbide and nitride MAX phases, Small Methods 4 (3) (2020), 1900780, https://doi.org/10.1002/smtd.201900780.

[16] Z. Zhang, X. Duan, D. Jia, Y. Zhou, S. van der Zwaag, On the formation mechanisms and properties of MAX phases: a review, J. Eur. Ceram. Soc. 41 (7) (2021) 3851–3878, https://doi.org/10.1016/j.jeurceramsoc.2021.02.002.

[17] A. Zhou, Y. Liu, S. Li, X. Wang, G. Ying, Q. Xia, P. Zhang, From structural ceramics to 2D materials with multi-applications: a review on the development from MAX phases to MXenes, J. Adv. Ceram. 10 (6) (2021) 1194–1242, https://doi.org/10.1007/s40145-021-0535-5.

[18] H. Khaleghi, A. Eshaghi, Fabrication of superhydrophobic micro-nano structure Al_2O_3-13%TiO_2/PTFE coating with anti- fuoling and self-cleaning properties, Surf. Interfaces 20 (2020), 100559, https://doi.org/10.1016/j.surfin.2020.100559.

[19] S. Özer, E. Vural, S. Özel, Effects of fusel oil use in a thermal coated engine, Fuel 306 (2021), 121716, https://doi.org/10.1016/j.fuel.2021.121716.

[20] P.G. Lashmi, P.V. Ananthapadmanabhan, G. Unnikrishnan, S.T. Aruna, Present status and future prospects of plasma sprayed multilayered thermal barrier coating systems, J. Eur. Ceram. Soc. 40 (8) (2020) 2731–2745, https://doi.org/10.1016/j.jeurceramsoc.2020.03.016.

[21] C. Ma, W. Yu, G. Ma, W. Haidou, Recent progress on high temperature radar absorbing coatings (RACs): a review, Crit. Rev. Solid State Mater. Sci. (2022) 1–28, https://doi.org/10.1080/10408436.2022.2118663.

[22] T. Ren, L.N. Nforbi, R. Kanakala, O.A. Graeve, Phase stability and mechanisms of transformation of la-doped gamma-alumina, Inorg. Chem. 57 (6) (2018) 3035–3041, https://doi.org/10.1021/acs.inorgchem.7b02635.

[23] K.A. Matori, L.C. Wah, M. Hashim, I. Ismail, M.H. Zaid, Phase transformations of alpha-alumina made from waste aluminum via a precipitation technique, Int. J. Mol. Sci. 13 (12) (2012) 16812–16821, https://doi.org/10.3390/ijms131216812.

[24] W. Zeng, N. Chen, Q. Chen, Thermodynamics of thermal decomposition of aluminum hydroxide, Trans. Nonferrous Met. Soc. China 7 (3) (1997) 132–134.

[25] Q. Chen, W. Zeng, X. Chen, S. Gu, G. Yang, H. Zhou, Z. Yin, Investigation of the thermodynamic properties of γ-Al_2O_3, Thermochim. Acta 253 (1995) 33–39, https://doi.org/10.1016/0040-6031(94)01969-n.

[26] P. Wang, G. Ma, F. Su, W. Guo, S. Chen, H. Zhao, M. Liu, H. Wang, Microstructure and micromechanical properties of in situ synthesized TiO_{2-x} coatings by plasma spraying of bimodal feedstocks, J. Therm. Spray Technol. 31 (8) (2022) 2300–2313, https://doi.org/10.1007/s11666-022-01449-2.

[27] Z. Oo, I.M. Low, B.H. O'Connor, Dynamic study of the thermal stability of impure Ti_3SiC_2 in argon and air by neutron diffraction, Phys. B: Condens. Matter 385– 386 (2006) 499–501, https://doi.org/10.1016/j.physb.2006.05.255.

[28] N. Atazadeh, M. Saeedi Heydari, H.R. Baharvandi, N. Ehsani, Reviewing the effects of different additives on the synthesis of the Ti_3SiC_2 MAX phase by mechanical alloying technique, Int. J. Refract. Met. Hard Mater. 61 (2016) 67–78, https://doi.org/10.1016/j.ijrmhm.2016.08.003.

[29] H. Chen, Z. Huang, Y. Huang, Y. Zhang, Z. Ge, W. Ma, T. Zhang, M. Wu, S. Xu, F. Fan, S. Chang, Y. Chen, Consecutively strong absorption from gigahertz to terahertz bands of a monolithic three-dimensional Fe_3O_4/graphene material, ACS Appl. Mater. Interfaces 11 (1) (2019) 1274–1282, https://doi.org/10.1021/acsami.8b17654.

[30] C. Wu, J. Wang, X. Zhang, L. Kang, X. Cao, Y. Zhang, Y. Niu, Y. Yu, H. Fu, Z. Shen, K. Wu, Z. Yong, J. Zou, B. Wang, Z. Chen, Z. Yang, Q. Li, Hollow gradient-structured iron-anchored carbon nanospheres for enhanced electromagnetic wave absorption, Nano-Micro Lett. 15 (1) (2022) 7, https://doi.org/10.1007/s40820-022-00963-w.

[31] M.W. Barsoum, I. Salama, T. El-Raghy, J. Golczewski, H.J. Seifert, F. Aldinger, W. D. Porter, H. Wang, Thermal and electrical properties of Nb_2AlC, (Ti, Nb)$_2$AlC and Ti_2AlC, Metall. Mater. Trans. A 33 (9) (2002) 2775–2779, https://doi.org/10.1007/s11661-002-0262-7.

[32] S.T. Ahams, A. Shaari, R. Ahmed, N.F.A. Pattah, M.C. Idris, B.U. Haq, Ab initio study of the structure, elastic, and electronic properties of $Ti_3(Al_{1-n}Si_n)C_2$ layered ternary compounds, Sci. Rep. 11 (1) (2021) 4980, https://doi.org/10.1038/s41598-021-84466-5.

[33] M. Malki, C.M. Hoo, M.L. Mecartney, H. Schneider, W.C.Jimmy Wei, Electrical conductivity of mullite ceramics, J. Am. Ceram. Soc. 97 (6) (2014) 1923–1930, https://doi.org/10.1111/jace.12867.

[34] J. Kita, F. Schubert, F. Rettig, A. Engelbrecht, A. Groß, R. Moos, Ceramic alumina substrates for high-temperature gas sensors-implications for applicability, Procedia Eng. 87 (2014) 1505–1508, https://doi.org/10.1016/j.proeng.2014.11.584.

[35] R.J. Coelho, Physics of Dielectrics for the Engineer. Amsterdam-Oxford-New York, Elsevier Scientific Publishing Company,, 1979.

[36] A.K. Jonscher, Dielectric Relaxation in Solids, Chelsea Dielectric Press,, London, 1983.

[37] B. Zhao, X. Guo, W. Zhao, J. Deng, G. Shao, B. Fan, Z. Bai, R. Zhang, Yolk–shell Ni@SnO_2 composites with a designable interspace to improve the electromagnetic wave absorption properties, ACS Appl. Mater. Interfaces 8 (42) (2016) 28917–28925, https://doi.org/10.1021/acsami.6b10886.

[38] M.H. Khan, S. Pal, E. Bose, Frequency-dependent dielectric permittivity and electric modulus studies and an empirical scaling in (100−x)$BaTiO_3$/(x) $La_{0.7}Ca_{0.3}MnO_3$ composites, Appl. Phys. A 118 (3) (2014) 907–912, https://doi.org/10.1007/s00339-014-8810-8.

[39] J. Malecki, B. Hilczer, Dielectric behaviour of polymers and composites, Key Eng. Mater. 92– 93 (1994) 181–216, https://doi.org/10.4028/www.scientific.net/KEM.92-93.181.

[40] J. Su, W. Zhou, Y. Liu, Y. Qing, F. Luo, D. Zhu, Effect of Ti_3SiC_2 addition on microwave absorption property of Ti_3SiC_2/cordierite coatings, Surf. Coat. Technol. 270 (2015) 39–46, https://doi.org/10.1016/j.surfcoat.2015.03.021.

[41] Y. Liu, Y. Li, F. Luo, X. Su, J. Xu, J. Wang, X. He, Y. Qu, Electromagnetic and microwave absorption properties of SiO_2-coated Ti_3SiC_2 powders with higher oxidation resistance, J. Alloys Compd. 715 (2017) 21–28, https://doi.org/10.1016/j.jallcom.2017.04.301.

[42] Y. Liu, J. Qin, L. Lu, J. Xu, X. Su, Enhanced microwave absorption property of silver decorated biomass ordered porous carbon composite materials with frequency selective surface incorporation, Int. J. Miner., Metall. Mater. 30 (3) (2023) 525–535, https://doi.org/10.1007/s12613-022-2491-7.

[43] C. Ji, Y. Liu, J. Xu, Y. Li, Y. Shang, X. Su, Enhanced microwave absorption properties of biomass-derived carbon decorated with transition metal alloy at improved graphitization degree, J. Alloys Compd. 890 (2022), 161834, https://doi.org/10.1016/j.jallcom.2021.161834.

[44] N. Wu, X. Liu, C. Zhao, C. Cui, A. Xia, Effects of particle size on the magnetic and microwave absorption properties of carbon-coated nickel nanocapsules, J. Alloys Compd. 656 (2016) 628–634, https://doi.org/10.1016/j.jallcom.2015.10.027.

[45] Z. Ma, C. Cao, Q. Liu, J. Wang, A new method to calculate the degree of electromagnetic impedance matching in one-layer microwave absorbers, Chin. Phys. Lett. 29 (3) (2012), 038401, https://doi.org/10.1088/0256-307x/29/3/038401.